Soft Matter

PAPER

View Article Online
View Journal | View Issue

Cite this: *Soft Matter*, 2025, 21, 6550

Dielectrophoretic response and electro-deformation of soft bioparticles interacting with a metallo-dielectric Janus active particle†

Donggang Cao[a] and Gilad Yossifon *[ab]

Received 7th May 2025,
Accepted 22nd July 2025

DOI: 10.1039/d5sm00462d

rsc.li/soft-matter-journal

Active (self-propelling) particles have emerged as innovative microscale tools in the field of single cell analysis with the advantages of being untethered, remotely controlled, hybrid powered, with sub-cellular precision. This study investigates the dielectrophoretic (DEP) response and electro-mechanical deformation of cell nuclei interacting with active metallo-dielectric Janus Particles (JPs) under an externally applied electric field. An "equivalent droplet" two-phase model is employed to simulate the bioparticle, coupling the Navier–Stokes equations with the phase field model to capture fluid motion and interface dynamics. Good qualitative agreement is obtained among experimental, analytical, and numerical results. The findings reveal a nonlinear relationship between nucleus deformation and its surface coverage of the JP with respect to the applied voltage. The overall coverage ratio of the JP's dielectric hemisphere increases with voltage as the positive DEP force on the dielectric side strengthens, exhibiting a maximum at a certain voltage. The strong correlation between nucleus flexibility and JP surface coverage suggests that the JP coverage ratio could serve as a biomechanical marker for nucleus deformability, providing a novel method for *in situ* evaluation of nucleus mechanics.

1. Introduction

Self-propelling micromotors have garnered significant attention in recent years for their potential as innovative microscale tools in single-cell analysis.[1–3] These micromotors enable precise manipulation[4] and probing of individual cells[5] and subcellular components,[6] advancing various biomedical applications.[7,8] Among the diverse range of micromotors and powering mechanisms,[9–14] electrically powered metallo-dielectric Janus particles (JPs) have emerged as particularly useful due to their simple fabrication and the advantages of electrical actuation—being fuel-free, label-free, biocompatible, and easily controlled by adjusting the electric field magnitude and frequency. These properties enable complex electrokinetic JP actuations[15–17] and make them particularly advantageous for label-free dielectrophoretic (DEP) manipulations, where DEP forces[18,19] and electro-deformation effects[20,21] can be harnessed to manipulate soft bioparticles, such as cell nuclei,[22] with high precision. These capabilities open new possibilities in targeted drug delivery,[23] cell sorting,[24] and single-cell mechanical characterization.[25]

The asymmetric design of JPs allows them to function as mobile microelectrodes under an applied electric field, generating localized field gradients that drive DEP forces.[26] These forces can trap and deform soft bioparticles, providing a dual mechanism for both manipulation and mechanical assessment.[27] The electro-deformation of trapped cells and nuclei under DEP forces offers valuable insights into cellular mechanics, which are critical for understanding cellular health, disease mechanisms, and mechanical phenotyping—that is, the assessment of structural integrity and mechanical properties in both healthy and diseased cells.[28,29] Notably, the nucleus, as the largest and mechanically dominant organelle in most cells, plays a central role in this context. Its deformability has been shown to correlate with metastatic potential, chromatin organization, and a range of disease states such as laminopathies and cancers.[30,31] These findings highlight the potential of electric-field-based probing to reveal biologically meaningful information about the mechanical behavior of soft bioparticles such as nuclei and whole cells.

While experimental studies have provided valuable preliminary insights into JP-bioparticle interactions, intriguing phenomena such as JP insertion and engulfment at cell membranes have been observed.[32,33] Our recent work has demonstrated that active, polarizable metallo-dielectric JPs effectively function as mobile microelectrodes, generating the necessary field gradients for efficient DEP manipulation.[34] Furthermore, we have highlighted the strong correlation between

[a] *School of Mechanical Engineering, Tel-Aviv University, Tel-Aviv, 69978, Israel. E-mail: gyossifon@tauex.tau.ac.il*
[b] *Department of Biomedical Engineering, Tel-Aviv University, Tel-Aviv, 69978, Israel*

† Electronic supplementary information (ESI) available. See DOI: https://doi.org/10.1039/d5sm00462d

DEP-induced electro-deformation of cell nuclei and applied field strength, underscoring the potential of JPs as active carriers for mechanical probing of subcellular components.[35] However, to the best of our knowledge, no systematic simulation studies have been conducted to investigate these complex JP-bioparticle interactions, particularly in DEP-based applications. This gap hinders the comprehensive interpretation of experimental data and the optimization of JP-bioparticle interactions for practical biomedical use. To address this gap, the present study employs numerical simulations using COMSOL Multiphysics 6.2[36] to analyse the DEP-driven interactions between JPs and deformable particles, with a particular focus on cell nuclei. Both the Janus particle and nucleus are modeled as spheres with 10 μm diameters. To simulate nucleus deformation under varying electric fields, we adopt an 'equivalent droplet' two-phase model that combines the properties of the cytoplasm and membrane (thickness $\sim$10 nm)[37–41] (see Section 2). This approach couples the Navier–Stokes equations with a phase-field method[42–44] to capture fluid dynamics and interface behavior, accounting for the interplay of hydrodynamic and electric forces driving nucleus motion and deformation.

The present study systematically investigates how particle composition, applied voltage, and nucleus stiffness influence dielectrophoretic response and electro-deformation. By providing a comprehensive framework for understanding these interactions, this research enhances fundamental physical insights, predictive modelling, and the design of DEP-based biomanipulation strategies, with broad implications for active particle-based biomedical applications.

2. Numerical simulation methodology

To simulate the JP-nucleus interaction, the incompressible Navier–Stokes equations are coupled with a multiphase framework to resolve fluid dynamics and track interface evolution under electric fields. In the analyzed microfluidic configuration, both continuous and dispersed phases exhibit laminar flow, with negligible influence from buoyancy and gravitational forces. The governing equations, incorporating electric stresses and surface tension, are formulated as:

$$\begin{cases} \rho\nabla\cdot\mathbf{u}=0 \\ \rho\dfrac{\partial\mathbf{u}}{\partial t}=\nabla\cdot[-p\mathbf{I}+\mu(\nabla\mathbf{u}+(\nabla\mathbf{u})^{T})]+\mathbf{F}_{\mathrm{st}}+\mathbf{F}_{\mathrm{e}} \end{cases} \tag{1}$$

where $\mathbf{u}$, $\mathbf{I}$, ρ, μ, p denote the velocity vector, identity tensor, density, dynamic viscosity, and pressure, respectively. $\mathbf{F}_{\mathrm{st}}$ represents the surface tension force, and $\mathbf{F}_{\mathrm{e}}$ denotes the Maxwell electric force.

To track the interface during the transient evolution of two-phase laminar flow, the phase-field method is employed for its efficiency in accurately capturing interface deformation under complex force interactions:[45,46]

$$\begin{cases} \dfrac{\partial\phi}{\partial t}+\mathbf{u}\cdot\nabla\phi=\nabla\cdot\dfrac{3\chi\gamma\xi}{2\sqrt{2}}\nabla\psi \\ \psi=-\nabla\cdot\xi^{2}\nabla\phi+(\phi^{2}-1)\phi \end{cases} \tag{2}$$

where ϕ is the phase-field variable, and it is -1 in the dispersed phase (nucleus) and 1 in the continuous phase (surrounding medium), γ denotes the surface tension coefficient. The numerical parameter, ξ, determines the thickness of the fluid interface where the phase-field variable ϕ varies from -1 to 1 smoothly, and χ is the interface mobility coefficient—an internal COMSOL numerical parameter that governs the diffusion rate of ϕ across the interface.

The density and viscosity are automatically calculated from the phase-field variable ϕ:

$$\begin{cases} \rho=\rho_{\mathrm{n}}f_{\mathrm{n}}+\rho_{\mathrm{s}}f_{\mathrm{s}} \\ \mu=\mu_{\mathrm{n}}f_{\mathrm{n}}+\mu_{\mathrm{s}}f_{\mathrm{s}} \end{cases} \tag{3}$$

where the subscripts "n" and "s" indicate the nucleus and the solution, respectively. The volume fractions of the nucleus phase are $f_{\mathrm{n}}=(1-\phi)/2$, and the volume fraction of the solution phase is $f_{\mathrm{s}}=(1+\phi)/2$, which satisfies $f_{\mathrm{n}}+f_{\mathrm{s}}=1$. This guarantees mass conservation and ensures that the physical properties (*e.g.*, density and viscosity) vary continuously across the interface rather than abruptly, which is essential for numerical stability in simulations.

The surface tension force is calculated as:

$$\begin{cases} \mathbf{F}_{\mathrm{st}}=G\nabla\phi \\ G=\dfrac{3\gamma\xi}{2\sqrt{2}}\left[-\nabla^{2}\phi+\dfrac{(\phi^{2}-1)\phi}{\xi^{2}}\right] \end{cases} \tag{4}$$

The electric force is given by the divergence of the Maxwell stress tensor by the equation below:[47,48]

$$\begin{cases} \mathbf{F}_{\mathrm{e}}=\nabla\cdot T \\ \mathbf{T}=\mathbf{E}\mathbf{D}^{T}-[(\mathbf{E}\cdot\mathbf{D})\mathbf{I}]/2 \end{cases} \tag{5}$$

wherein $\mathbf{E}$ is the electric field and $\mathbf{D}$ is the electric displacement field with the following expressions:

$$\begin{cases} \mathbf{E}=-\nabla V \\ \mathbf{D}=\varepsilon\mathbf{E} \end{cases} \tag{6}$$

Furthermore, the current conservation equation can be solved to determine $\mathbf{E}$:

$$\begin{cases} \nabla\cdot\left(\varepsilon\dfrac{\partial\mathbf{E}}{\partial t}+\sigma\mathbf{E}\right)=0 \\ \varepsilon=\varepsilon_{\mathrm{n}}f_{\mathrm{n}}+\varepsilon_{\mathrm{s}}f_{\mathrm{s}} \\ \sigma=\sigma_{\mathrm{n}}f_{\mathrm{n}}+\sigma_{\mathrm{s}}f_{\mathrm{s}} \end{cases} \tag{7}$$

where ε is the permittivity and σ is the conductivity.

Directly solving these equations in the physical time domain to simulate nucleus deformation at 1 MHz requires prohibitively small time steps and incurs high computational costs. To balance efficiency and accuracy, the electrical problem is solved in the frequency domain, and a cycle-averaged electric force is applied in the time domain.[49] This is an appropriate approximation given the significant disparity in timescales between fluid motion ($\sim$ms) and electrical excitation ($\sim$MHz). Consequently, the governing equation for the electric field in the

frequency domain becomes:

$$\begin{cases} \nabla \cdot \left(i\omega\varepsilon\tilde{\mathbf{E}} + \sigma\tilde{\mathbf{E}}\right) = 0 \\ \varepsilon = \varepsilon_{\mathrm{n}} f_{\mathrm{n}} + \varepsilon_{\mathrm{s}} f_{\mathrm{s}} \\ \sigma = \sigma_{\mathrm{n}} f_{\mathrm{n}} + \sigma_{\mathrm{s}} f_{\mathrm{s}} \end{cases} \tag{8}$$

while the cycle-averaged force is formulated as:[50]

$$\begin{cases} \langle \mathbf{F}_{\mathrm{e}} \rangle = \nabla \cdot \langle \mathbf{T} \rangle \\ \langle \mathbf{T} \rangle = 0.25\mathrm{Re}(\tilde{\varepsilon}) \left[\left(\tilde{\mathbf{E}}\tilde{\mathbf{E}}^{*} + \tilde{\mathbf{E}}^{*}\tilde{\mathbf{E}} \right) - \left\| \tilde{\mathbf{E}} \right\|^{2} \mathbf{I} \right] \end{cases} \tag{9}$$

Here, the tilde "$\sim$" denotes complex phasor quantities, and the asterisk (*) denotes the complex conjugate of the phasor $\tilde{\mathbf{E}}$. Only the real part of the medium complex permittivity $\mathrm{Re}(\tilde{\varepsilon}) = \varepsilon$ appears in the Maxwell stress tensor because it represents the in-phase component responsible for energy storage and electrostatic forces, while the imaginary part relates to losses and does not affect the time-averaged stress.

The cell nucleus is modelled as a homogenized "equivalent droplet" with effective electrical properties that capture the combined influence of the nucleus membrane and nucleus cytoplasm, as illustrated in Fig. S1 (ESI†). The characteristic dielectric properties of the nucleus membrane and cytoplasm, obtained from the literature, are summarized in Table S1 (ESI†). The DEP response across a broad frequency range, evaluated using the Clausius–Mossotti factor, is presented in Fig. S2 (ESI†). Table S2 (ESI†) provides the physical properties of the nucleus and the surrounding fluid, selected to satisfy the experimental condition that a positive DEP (pDEP) force arises at the experimentally investigated frequency of 1 MHz.

The governing equations are solved with the following boundary conditions: the upper and lower walls act as electrodes with applied voltages, while the left and right channel edges are set to electric insulation. Since our primary focus is on simulating the high frequency domain ($\sim$1 MHz), consistent with the preliminary experiments,[35] we neglect induced-charge electro-osmosis (ICEO) effects and the effective Helmholtz-Smoluchowski slip boundary condition on the metal hemisphere. This simplification is justified as the operating frequency is significantly higher than the RC frequency associated with the formation of the induced electrical double layer (EDL) ($f_{\mathrm{RC}} = 1/2\pi\tau = 1.3$ kHz refers to the characteristic charging frequency, where $\tau = \lambda R/D$ is the induced charge relaxation time; $R = 5$ μm is the radius of JP; $\lambda = \sqrt{\varepsilon_{\mathrm{s}} D/\sigma}$ is the Debye length; $\sigma = 6 \times 10^{-4}$ S m^{-1} is the solution conductivity; $\varepsilon_{\mathrm{s}} = 78\varepsilon_0$ is the solution permittivity and $\varepsilon_0 = 8.854187817 \times 10^{-12}$ F m^{-1} is the vacuum permittivity; $D = 2 \times 10^{-9}$ m^2 s^{-1} is the diffusion coefficient of the ionic species[51]). Accordingly, the JP is modeled by assigning distinct boundary conditions to its two hemispheres: a floating electrode condition for the metallic (gold) hemisphere and an insulating condition for the dielectric (polystyrene) hemisphere.[34] Validation results in the ESI† confirm that the applied boundary conditions effectively capture JP–nucleus interactions at 1 MHz (see Fig. S3 and S4, ESI†). Additionally, Fig. S5 (ESI†) presents the Clausius–Mossotti factor and the corresponding JP–nucleus interaction, derived from the parameters in Table S2 (ESI†) and simulations using the floating boundary condition. These results indicate that, as frequency increases beyond 1 MHz—where positive dielectrophoresis (pDEP) is observed experimentally—a transition to negative DEP (nDEP) occurs, leading the nucleus to migrate toward regions of lower electric field strength. The strong agreement between analytical predictions and numerical simulations further supports the validity and robustness of the proposed modeling approach.

In addition, no-slip boundary conditions are imposed on all solid walls, which is justified at the examined frequency ($\sim$1 MHz), well above the RC frequency $f_{\mathrm{RC}} = 1/2\pi\tau = 1.3$ kHz. A time-dependent solver is used to capture the dynamic JP–nucleus interaction, with the focus placed on the quasi-steady-state results, as illustrated in Fig. S6 (ESI†). To accurately resolve the complex interactions in the system, second-order numerical schemes are employed in conjunction with a locally refined mesh (see Fig. S7, ESI†), concentrating computational effort in regions with steep field gradients. Four computational grids with varying cell counts (see Table S3, ESI†) are used to assess numerical errors arising from limited spatial resolution. The results confirm that a fine mesh with approximately 30 000 cells provides accurate and grid-independent solutions. Further details on the grid-independence validation are provided in Fig. S8 of the ESI.†

3. Results and discussion

3.1. Overview of JP-nucleus interaction

Our previously studied experimental setup[33] consists of a simple microfluidic chamber, formed by positioning a 120 μm-high space between two parallel indium tin oxide (ITO)-coated glass substrates. JPs consisting of gold half-coated polystyrene spherical particles, are introduced into the chamber along with target cell nuclei. The manipulation and transport of the JPs are controlled by an externally applied electric field, as schematically illustrated in Fig. 1A. Fig. 1B schematically represents the nucleus as a homogeneous "equivalent droplet" incorporating the combined properties of the nucleus's cytoplasm and membrane.

When exposed to an electric field, the JP attracts and deforms the nucleus onto its surface, enabling it to carry and transport the loaded nucleus[35] (Fig. 1C, the reduced contrast of the nucleus in the final experimental frame is due to a slight displacement in the z-direction during interaction, causing the nucleus to move partially out of the focal plane). Fig. 1D shows numerical simulation snapshots (a cross-sectional view of plane A–A in Fig. 3A) illustrating the JP-nucleus interaction over time. The nucleus is attracted to the JP by DEP forces, gradually deforming and migrating until it reaches a steady-state shape, settling on the JP's surface and covering parts of both the gold and polystyrene hemispheres. The initial spacing between the JP and the nucleus was set arbitrarily at 2.5 μm. This behaviour aligns qualitatively with experimental observations (see Movie S1 in the ESI†) though there is an orientation mismatch.

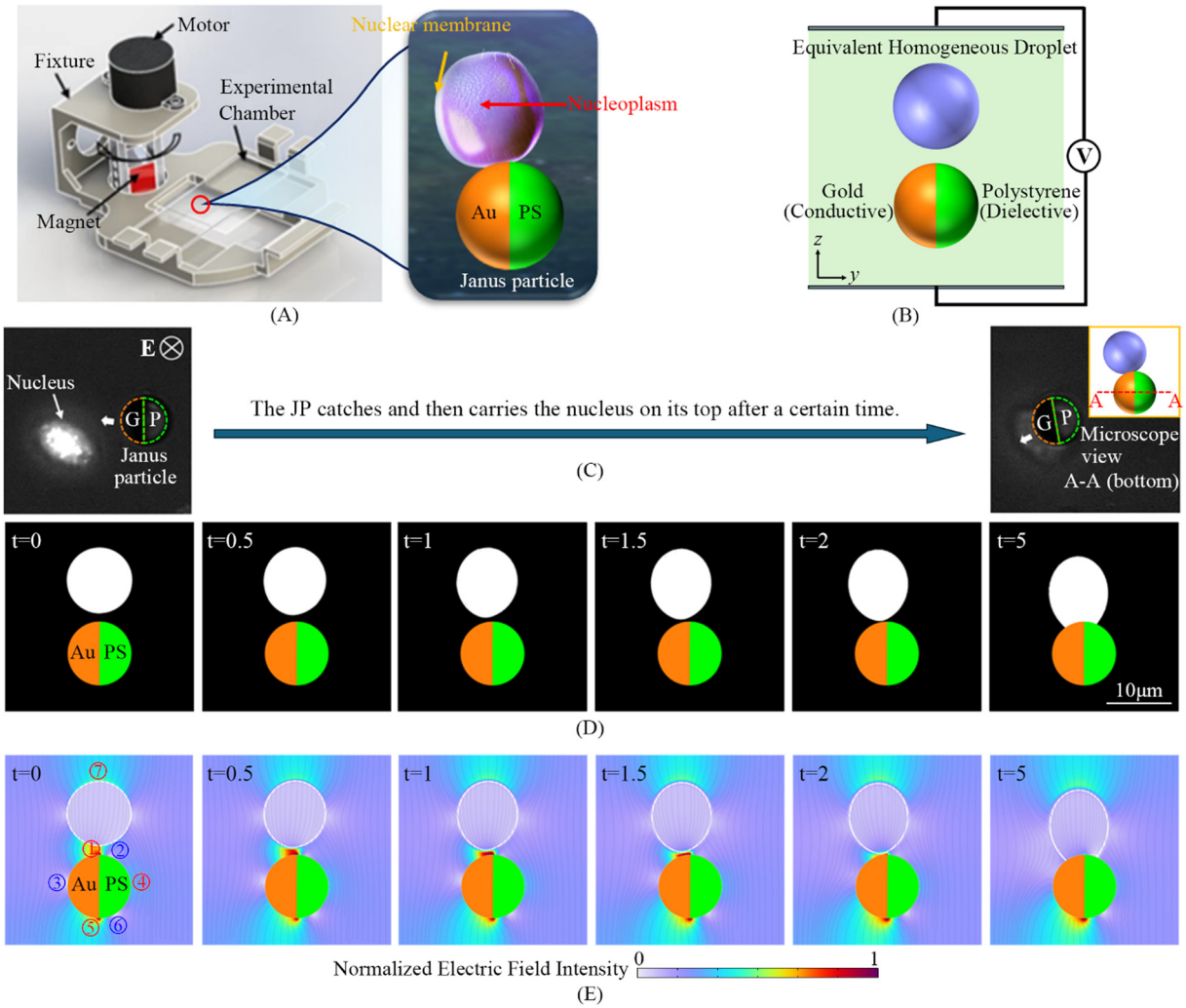

Fig. 1 Experimental and numerical system setups and overview of JP-nucleus interactions: (A) schematic of the experimental setup[35] (Copyright 2020 John Wiley and Sons). (B) Schematic representation of the simulation model. (C) Time evolution of JP-nucleus interaction observed experimentally, showing nucleus attraction and deformation onto the JP (inset: side-view schematic)[35] (Copyright 2020 John Wiley and Sons). (D) Corresponding numerical simulation snapshots. (E) Normalized electric field intensity distributions at different normalized (scaled by the characteristic DEP migration time t_s = 3.1 ms at V_{pp} = 10 V, f = 1 MHz, see ESI,† for more details) time points (white line indicates the nucleus surface contour).

Fig. 1E presents the time-evolving normalized electric field distribution, further supporting the experimental findings. Both nucleus and JP undergo polarization in the electric field, with the JP inducing perturbations that generate distinct dielectrophoretic (DEP) potential wells, labelled ①–⑥ in the first panel of Fig. 1E. Local maxima in the electric field at locations ① and ⑤ indicate regions where positive DEP (pDEP) trapping of bioparticles is likely, while a weaker pDEP well appears on the polystyrene side at location ④. Conversely, locations ②, ③, and ⑥ correspond to negative DEP (nDEP) trapping sites due to local electric field minima. The electric field asymmetry arises from the Janus particle's intrinsic surface asymmetric dielectric properties (gold *vs.* polystyrene, where the former is ideally polarizable while the latter is insulating) in contrast with a homogenous particle where symmetry does exist. In response to a positive dielectrophoresis (pDEP) force,[35] the nucleus, behaving as a homogeneous dielectric droplet, moves toward the high-intensity potential well at location ①. Upon contact with the JP, the electric field intensity at the JP-nucleus interface (location ①) gradually decreases until the system reaches a steady-state deformed nucleus configuration.

3.2. Interactions between nuclei and different particles

The spatial variation of induced dielectrophoretic (DEP) potential wells on the JP's surface plays a crucial role in governing JP-nucleus interactions, depending on their relative positioning. To further investigate this, we conducted a comparative numerical analysis of interactions involving four nuclei positioned around three types of particles: homogeneously conductive, homogeneously dielectric, and Janus (Fig. 2). The conductive gold particle exhibits positive DEP trapping at the top and bottom, while negative DEP regions appear on its lateral sides, whereas the dielectric particle shows the opposite behaviour. Consequently, nuclei above or below

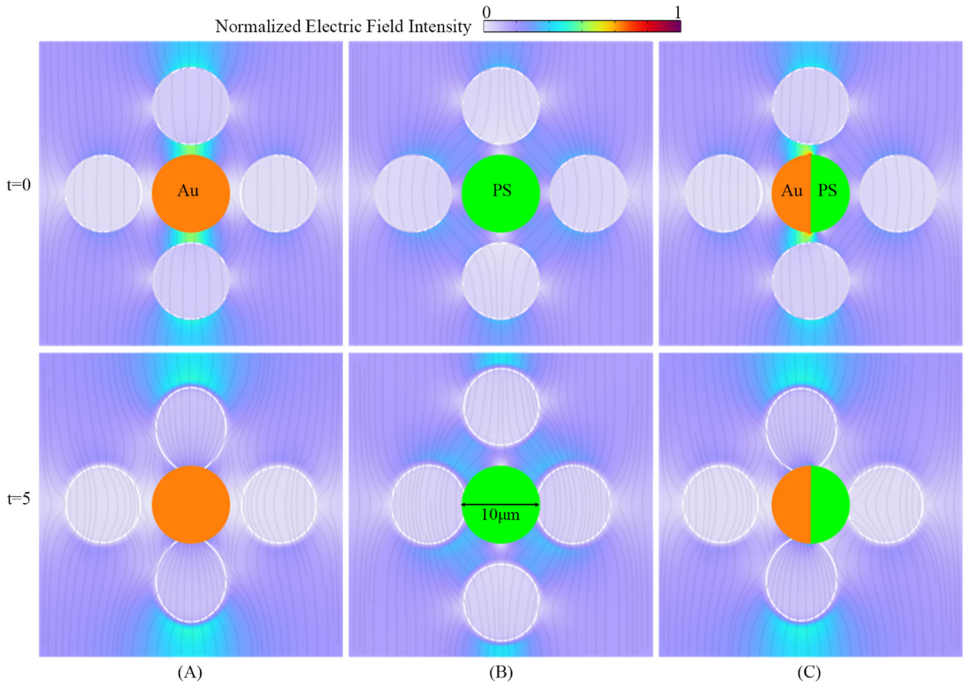

Fig. 2 Normalized electric field distributions (scaled by 10^6 V m^{-1}) are shown for nuclei positioned at various locations around (A) a conductive particle, (B) a dielectric particle, and (C) a Janus particle at different normalized time points (scaled by the characteristic DEP migration time t_s = 3.1 ms at V_{pp} = 10 V, f = 1 MHz, see ESI,† for more details).

the gold particle are attracted to it, while those on the lateral sides experience repulsion, and *vice versa* for the dielectric particle. Interactions with the JP combines the effects of both the gold (conductive) and dielectric particles. Nuclei located above or below the JP predominantly migrate toward the conductive side due to positive DEP, while nuclei adjacent to the conductive lateral surface are repelled, and those near the dielectric side are attracted. The hybrid nature of the JP thus enables complex, spatially selective interactions with target nuclei.

The electric field distributions in Fig. 2A and B exhibit bilateral (mirror) symmetry about the vertical axis due to the uniform material properties of the conductive (Au) and dielectric (PS) particles, respectively. This symmetry is preserved from the initial state to the quasi-steady state, resulting in symmetric field lines and DEP forces acting radially and evenly around the particle. In contrast, the Janus particle in Fig. 2C introduces asymmetry due to the distinct material properties of its Au and PS hemispheres. This breaks the mirror symmetry of the field distribution, concentrating electric field gradients near the metallo-dielectric interface. As a result, the nucleus experiences a directional DEP force, leading to asymmetric migration and deformation. The comparison underscores the role of particle symmetry in governing field gradients and the resulting mechanical response of nearby soft particles.

3.3. Impact of the applied electric field on the Janus-nucleus interaction

Our previous experimental study[35] demonstrated that a nucleus trapped by a JP can spread onto the polystyrene (PS) hemisphere, with the extent of coverage directly correlated to the applied voltage. Fig. 3 provides a comprehensive analysis of this interaction, comparing experimental observations[35] with numerical simulations. Both 2D and 3D models are employed to simulate the JP-nucleus interaction. As shown in Fig. 3A, results from the central plane of interest (plane A–A, which is also shown in Fig. 1) in the 3D simulations closely align with those from the 2D simulations, confirming the viability of the 2D approach. Therefore, given the high computational cost and time demands of 3D simulations, we propose using the more efficient qualitative 2D simulations to systematically investigate the impact of the applied electric field on JP-nucleus interactions. Fig. 3B shows experimental images[35] of the nucleus (in red) and the JP surface (outlined by a dotted yellow circle) at 4 V and 18 V. The increasing coverage of the JP's PS hemisphere by the nucleus (shaded sector) indicates enhanced electro-deformation under higher electric fields. Besides, the nucleus at 18 V becomes narrower than at 4 V, indicating that the nucleus becomes more ellipsoidal in the stronger electric field. The corresponding simulation snapshots in Fig. 3C further support the experimental observation, showing increased nucleus coverage on the PS hemisphere as voltage rises. The agreement between experimental and numerical results validates the simulation approach, reinforcing its utility for further analysis.

Fig. 3D illustrates the electric field magnitude distribution around the JP and nucleus at different voltages, demonstrating how the field evolves as the applied voltage increases. As described in Section 2.1, the nucleus experiences pDEP forces, migrating toward regions of higher electric field intensity. Initially, the strongest field intensity at location ① serves as the primary trapping site. However, as the nucleus is captured,

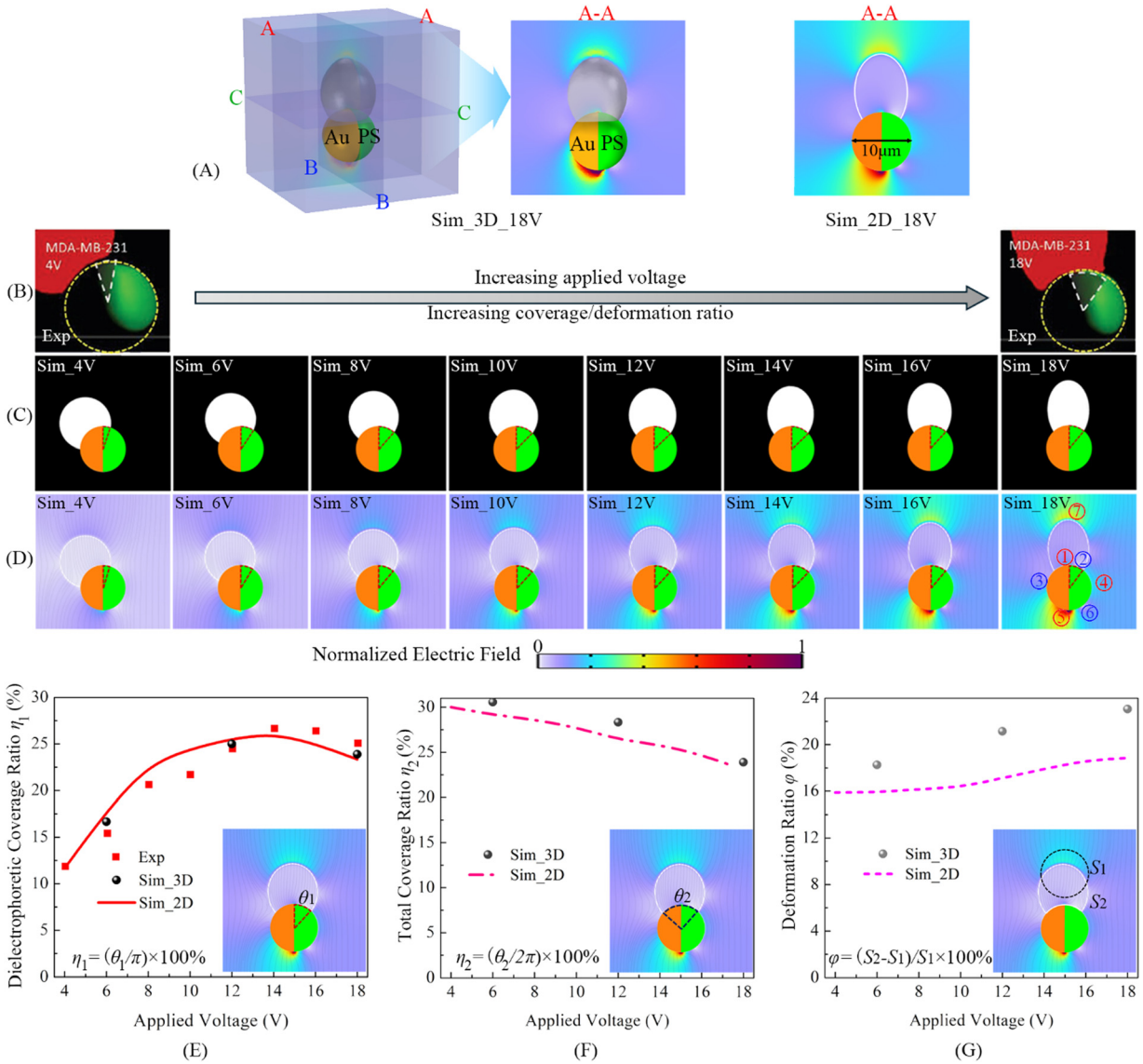

Fig. 3 JP-Nucleus interaction under varying electric fields at 1 MHz: (A) Comparison of 3D and 2D simulation results. (B) Experimental images of the nucleus (red) and Janus particle (JP, dotted yellow outline) reconstructed using Imaris 5.0[52] at the central plane. The green region represents the polystyrene (PS) hemisphere of the JP, while the shaded circular sector denotes the PS portion covered by the nucleus. The red color of the nucleus in the experimental image highlights its shape, as extracted from fluorescence microscopy[35] (Copyright 2020 John Wiley and Sons). (C) Numerical images of the nucleus (white) and JP, with the dashed circular sector indicating the PS hemisphere region covered by the nucleus. (D) Simulated electric field distributions during JP-nucleus interactions at different applied voltages. (E) Experimental and simulated dielectrophoretic coverage ratio of the PS hemisphere *versus* applied voltage. (F) Total coverage ratio (including both PS and Au hemispheres) *versus* applied voltage. (G) Deformation ratio of the nucleus *versus* applied voltage.

this pDEP well weakens, and other wells, particularly on the PS side (location ④), become more influential. The increasing field intensity at ④ at higher voltages enhances the nucleus's attraction to the polystyrene hemisphere.

The quantitative analysis of the dielectrophoretic coverage ratio (Fig. 3E), defined as the fraction of the JP's PS hemisphere covered by the nucleus ($\eta_1 = (\theta_1/\pi) \times 100\%$, where θ_1 is the angular coverage), further supports the validity of the 2D simulations. Despite the limited number of 3D data points due to computational constraints, both 2D and 3D simulations show good agreement with experimental results, using surface tension as the sole fitting parameter to the differing deformability of MDA-MB-231 and MCF-7 nuclei.

Generally, the coverage ratio increases with the applied voltage up to approximately 14 V, after which a slight decline is observed. This non-monotonic behaviour may result from competing mechanisms: on one hand, increased electric field intensity enhances pDEP-driven attraction toward location ④, promoting greater nucleus coverage of the dielectric side; on the other hand, elongation of the nucleus along the field lines reduces its effective contact area with the JP, thereby decreasing θ_1. This elongation also influences the total coverage ratio

($\eta_2 = (\theta_2/2\pi) \times 100\%$), which declines with increased voltages (Fig. 3F). Although the 2D simulations qualitatively match the 3D results on the plane of interest in terms of coverage ratios, they do not fully replicate the deformation ratio of the 3D system (Fig. 3G). The deformation ratio, defined as the percentage increase in the nucleus's surface area ($\varphi = (\Delta S/S) \times 100\%$), quantifies how much the nucleus stretches under the electric field. Since 2D simulations inherently capture deformation in only two directions, the deformation ratios are different from those from 3D simulations. Hence, while the 2D simulations have quantitative limitations in predicting deformation ratios, they provide valuable insights into the key mechanisms of JP-nucleus interaction.

3.4. Impact of the nuclei stiffness on the Janus-nucleus interaction

Nucleus deformability plays a critical role in shaping the interaction dynamics between a nucleus and a JP under an

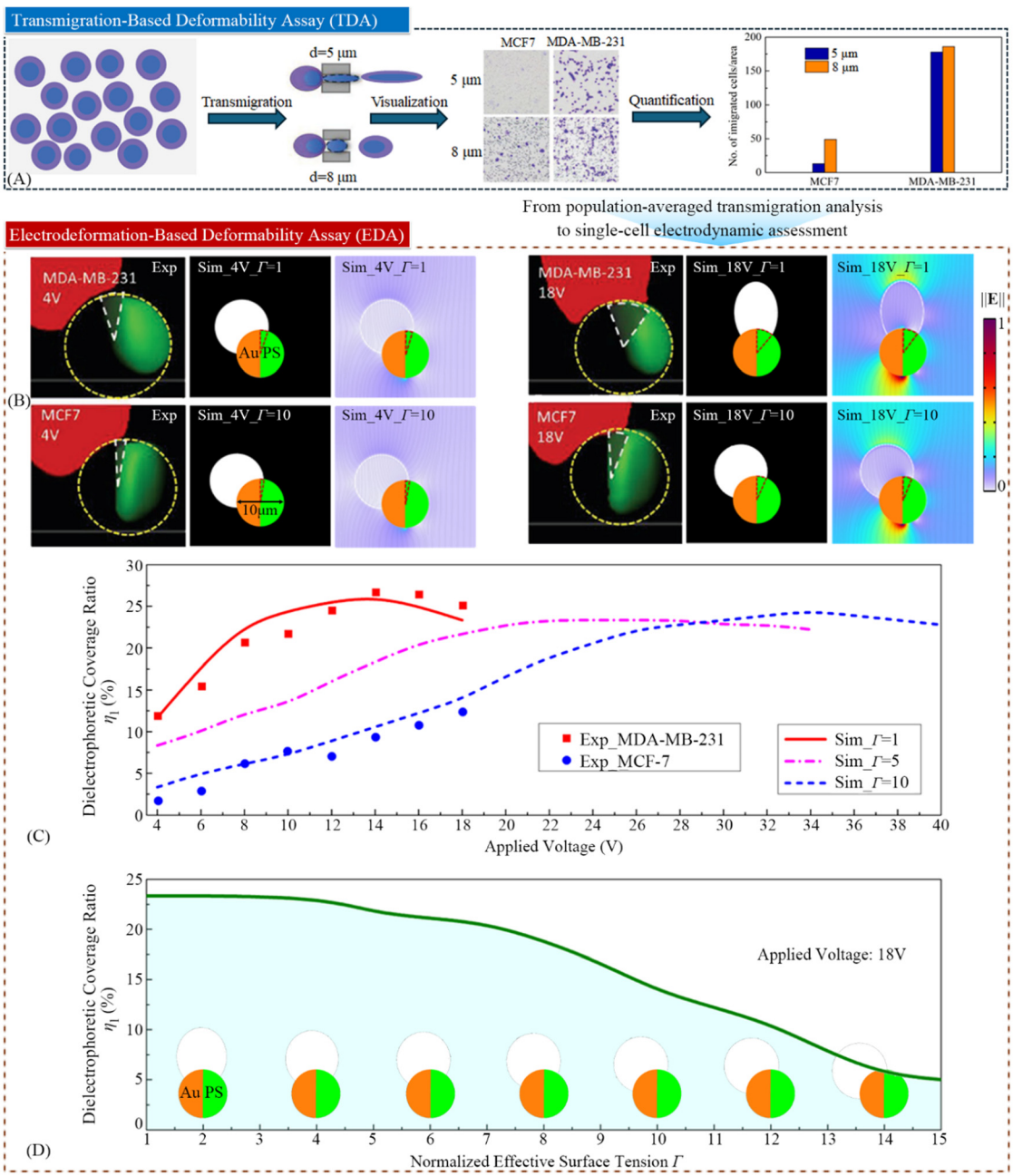

Fig. 4 Influence of nucleus stiffness on JP-nucleus interaction at 1 MHz: (A) schematic of the transmigration-based deformability assay (TDA) and results from ref. 35 (Copyright 2020 John Wiley and Sons) demonstrating the deformability of MDA-MB-231 and MCF-7 cells. (B) Comparison of experimental[35] (Copyright 2020 John Wiley and Sons) and numerical results for JP-nucleus interactions with varying nucleus stiffness (MDA-MB-231 and MCF-7) at 4 V and 18 V. (C) Simulated dielectrophoretic coverage ratio as a function of applied voltage for different nucleus stiffnesses (represented by equivalent surface tension, Γ); (D) simulated dielectrophoretic coverage ratio as a function of equivalent surface tension (Γ) at the applied voltage of 18 V.

applied electric field. To investigate this, we studied JP interactions with two cell nuclei of differing stiffness: the more deformable MDA-MB-231 nucleus and the stiffer MCF-7 nucleus. This distinction is biologically relevant, as increased nuclear deformability has been associated with enhanced migratory ability and metastatic potential in aggressive cancer cell lines such as MDA-MB-231,[53] though this correlation does not imply direct causation.

To quantify nucleus deformability, the transmigration-based deformability assay (TDA) using Transwell inserts with 5 μm and 8 μm pores was employed in ref. 35. In this assay, MDA-MB-231 cells – known for their high deformability - exhibited increased transmigration, with over 180 cells passing through both pore sizes. This high rate of passage suggests that their nuclei can easily deform and squeeze through narrow openings. In contrast, MCF-7 cells, with lower deformability, depict limited transmigration, with only about 50 cells passing through the 8 μm pores and very few through the 5 μm pores, highlighting the stiffness of their nuclei (Fig. 4A).

Correspondingly, simulations have been conducted by modelling the nucleus deformability through an effective surface tension parameter (γ). Fig. 4B presents experimental images and simulation snapshots comparing interactions of the JP with nuclei of varying deformability (represented by the normalized equivalent surface tension, $\Gamma = \gamma/\gamma_0$, with $\gamma_0 = 0.0002$ N m^{-1} (ref. 54)) at 4 V and 18 V. For the highly deformable MDA-MB-231 nuclei, simulations with lower Γ values (indicating higher deformability) show increased coverage of the JP's polystyrene side. Conversely, stiffer MCF-7 nuclei exhibit reduced coverage, in qualitative agreement with experimental observations. Fig. 4C quantifies the dielectrophoretic coverage ratio (η_1) as a function of applied voltage for nuclei with varying surface tension values. Across all deformability levels, η_1 increases with voltage, but the rate of increase is strongly influenced by nucleus stiffness. Softer nuclei (lower Γ values, *e.g.*, MDA-MB-231) exhibit a steep rise in η_1, indicating their greater ability to conform to the JP's surface under stronger electric fields. Conversely, stiffer nuclei (higher Γ values, *e.g.*, MCF-7) show a more gradual and limited increase in η_1, reflecting their resistance to deformation. All curves follow a similar trend: an initial rapid rise in η_1, followed by a reduced growth rate beyond a critical transition voltage. This transition voltage shifts higher for stiffer nuclei, highlighting the interplay between deformability and electric field strength.

Fig. 4D shows an inverse correlation between η_1 and Γ at 18 V and 1 MHz, indicating that stiffer nuclei (higher Γ) exhibit lower dielectrophoretic coverage due to reduced deformability. This suggests that JP coverage ratio may serve as a biomechanical marker of nucleus stiffness. Unlike the population-based TDA assay, which uses mechanical squeezing for indirect, high-throughput screening, our electro-deformation approach employs electrostatic forces for direct, single cell resolution. While TDA is simple and scalable, EDA offers quantitative, real-time insight into single-cell mechanics. Together, they provide complementary perspectives on nuclear deformability.

4. Conclusion

This study investigated the DEP response and electro-deformation of soft bioparticles, specifically cell nuclei, interacting with a metallo-dielectric JP under varying electric fields. Using numerical simulations validated against previous experimental observations, we analysed how applied voltage and nucleus deformability influence DEP-induced deformation and the extent of nucleus coverage on the JP surface. Our findings reveal a nonlinear relationship between the dielectrophoretic coverage ratio of the deformable nucleus on the JP's polystyrene hemisphere and the applied voltage. Initially, the coverage ratio increases with voltage, reaching a maximum before slightly declining at higher voltages. This behaviour arises from the dynamic interplay between the soft nucleus and the multiple potential wells formed around the JP's surface. At lower voltages, the strongest positive DEP (pDEP) well at the JP interface attracts and traps the nucleus. However, once the conductive nucleus attaches, this potential well weakens, allowing other pDEP wells—particularly the one on the polystyrene side—to dominate, pulling the nucleus in that direction and stretching it. Nucleus deformability plays a crucial role in modulating the JP-nucleus interaction. Highly deformable nuclei (*e.g.*, MDA-MB-231) exhibit greater coverage and adapt more readily to the JP surface, whereas stiffer nuclei (*e.g.*, MCF-7) show limited interaction due to their reduced ability to deform. These findings highlight the potential of JPs as microscale tools for probing nucleus deformability—a key mechanical biomarker associated with different cellular states and diseases. Since nucleus stiffness strongly influences electro-deformation, it enables selective manipulation and sorting of cells and their nuclei by controlling their loading and positioning on the JP surface. These findings offer valuable guidance for utilizing DEP forces in biomedical applications such as single-cell and organelle mechanical probing, sensing, and selective manipulation based on mechanical and dielectric properties.

Conflicts of interest

There are no conflicts to declare.

Data availability

The data supporting this article have been included as part of the ESI.†

Acknowledgements

The authors thank Dr Yue Wu and Dr Afu Fu for assistance with imaging and helpful discussions. G. Y. acknowledges support from the Israel Science Foundation (ISF) (1429/24). D. C. is grateful to Anna Juhasz from COMSOL for her technical support.

References

1 M. Guix, S. M. Weiz, O. G. Schmidt and M. Medina-Sánchez, *Part. Part. Syst. Charact.*, 2018, **35**, 1700382.
2 Y. Wang, J. Chen, G. Su, J. Mei and J. Li, *Micromachines*, 2023, **14**, 1710.
3 R. Maria-Hormigos, B. Jurado-Sánchez and A. Escarpa, *Lab Chip*, 2016, **16**, 2397.
4 E. B. Steager, M. S. Sakar, C. Magee, M. Kennedy, A. Cowley and V. Kumar, *Int. J. Robot. Res.*, 2013, **32**, 346.
5 D. Fu, J. Jiang, S. Fu, D. Xie, C. Gao, Y. Feng, S. Liu, Y. Ye, L. Liu, Y. Tu and F. Peng, *Adv. Healthcare Mater.*, 2023, **12**, 2300737.
6 H. Xin, N. Zhao, Y. Wang, X. Zhao, T. Pan, Y. Shi and B. Li, *Nano Lett.*, 2020, **20**, 7177.
7 J. Ou, K. Liu, J. Jiang, D. A. Wilson, L. Liu, F. Wang, S. Wang, Y. Tu and F. Peng, *Small*, 2020, **16**, 1906184.
8 N. Ruiz-González, D. Esporrín-Ubieto, I. Kim, J. Wang and S. Sánchez, *ACS Nano*, 2025, **19**, 8411.
9 S. Gangwal, O. J. Cayre, M. Z. Bazant and O. D. Velev, *Phys. Rev. Lett.*, 2008, **100**, 058302.
10 T. Mirkovic, N. S. Zacharia, G. D. Scholes and G. A. Ozin, *Small*, 2010, **6**, 159.
11 Y. Wu, T. Si, J. Shao, Z. Wu and Q. He, *Nano Res.*, 2016, **9**, 3747.
12 T. Xu, W. Gao, L. Xu, X. Zhang and S. Wang, *Adv. Mater.*, 2017, **29**, 1603250.
13 Z. Wu, J. Troll, H. Jeong, Q. Wei, M. Stang, F. Ziemssen, Z. Wang, M. Dong, S. Schnichels, T. Qiu and P. Fischer, *Sci. Adv*, 2018, **4**, eaat4388.
14 Y. Chen, K. Guo, L. Jiang, S. Zhu, Z. Ni and N. Xiang, *Talanta*, 2023, **4**, 123815.
15 A. Boymelgreen, G. Yossifon and T. Miloh, *Langmuir*, 2016, **32**, 9540.
16 E. Poggi and J. Gohy, *Colloid Polym. Sci.*, 2017, **295**, 2083.
17 H. Su, C.-A. Price, L. Jing, Q. Tian, J. Liu and K. Qian, *Mater. Today Bio*, 2019, **4**, 100033.
18 P. R. C. Gascoyne and J. Vykoukal, *Electrophoresis*, 2002, **23**, 1973.
19 N. A. Rahman, F. Ibrahim and B. Yafouz, *Sensors*, 2017, **17**, 449.
20 M. Torbati and K. Mozaffari, *Rev. Mod. Phys.*, 2022, **94**, 025003.
21 R. Pethig, *J. Electrochem. Soc.*, 2017, **164**, B3049.
22 A. Matsumoto, T. Kitazawa, Y. Hatori, H. Nakanishi, C. Watanabe, T. Takashima and M. Murakami, *Drug Discovery Ther.*, 2023, **17**, 104.
23 K. X. Tan, M. K. Danquah, J. Jeevanandam and A. Barhoum, *Pharmaceutics*, 2023, **15**, 423.
24 E. O. Adekanmbi and S. K. Srivastava, *Appl. Phys. Rev*, 2019, **6**, 041313.
25 T. C. Le, J. Zhai, W. Chiu, P. A. Tran and N. Tran, *Int. J. Nanomed.*, 2019, **23**, 6749.
26 Y. Wu, A. Fu and G. Yossifon, *Sci. Adv.*, 2020, **6**, eaay4412.
27 Y. Wu, S. Yakov, A. Fu and G. Yossifon, *Adv. Sci.*, 2023, **10**, 2204931.
28 Y. Wu, A. Fu and G. Yossifon, *Proc. Natl. Aacd. Sci. U. S. A.*, 2021, **118**, e2106353118.
29 J. Wang, Y. Dong, P. Ma, Y. Wang, F. Zhang, B. Cai, P. Chen and B. Liu, *Adv. Mater.*, 2022, **34**, 2201051.
30 A. D. Stephens, E. J. Banigan, S. A. Adam, R. D. Goldman and J. F. Marko, *MboC*, 2017, **28**, 1984.
31 P. Isermann and J. Lammerding, *Curr. Biol.*, 2013, **23**, R1113.
32 H. Ding and Y. Ma, *Nanoscale*, 2012, **4**, 1116.
33 Y. Gao and Y. Yu, *J. Am. Chem. Soc.*, 2013, **135**, 19047.
34 A. M. Boymelgreen, T. Balli, T. Miloh and G. Yossifon, *Nat. Commun.*, 2018, **9**, 760.
35 Y. Wu, A. Fu and G. Yossifon, *Small*, 2020, 1906682.
36 **https://www.comsol.com/release/6.2**.
37 R. B. Dickinson and T. P. Lele, *Curr. Opin. Biomed. Eng.*, 2023, **28**, 100483.
38 D. Shao, H. Levine and W. Rappe, *Proc. Natl. Aacd. Sci. U. S. A.*, 2012, **109**, 6851.
39 F. Ziebert and I. S. Aranson, *npj Comput. Mater.*, 2016, **2**, 16019.
40 M. Pavlin and D. Miklavčič, *Biophys. J.*, 2003, **85**, 719.
41 A. Morshed, P. Dutta, M. R. Hossan and R. Dillon, *Phys. Rev. Fluids*, 2018, **3**, 103702.
42 S. Zhou, T. Rabczuk and X. Zhuang, *Adv. Eng. Software*, 2018, **122**, 31.
43 S. Aland, S. Egerer, J. Lowengrub and A. Voigt, *J. Comput. Phys.*, 2014, **277**, 32.
44 C. Shi, C. Huang, P. N. Devreotes and P. A. Iglesias, *PLoS Comput. Biol.*, 2013, **9**, e1003122.
45 M. R. Mardani, D. D. Ganji and Kh Hosseinzadeh, *J. Mol. Liq.*, 2022, **346**, 117111.
46 V. Chirkov, G. Utiugov, P. Kostin and A. Samusenko, *Int. J. Multiphase Flow*, 2024, **177**, 104881.
47 S. L. Leung, Y. Lu, D. Bluestein and M. J. Slepian, *Ann. Biomed. Eng.*, 2016, **44**, 903.
48 O. Ghazian, K. Adamiak and G. S. P. Castle, *Colloids Surf., A*, 2013, **423**, 27.
49 C. Rosales and K. M. Lim, *Electrophoresis*, 2005, **26**, 2057.
50 X. Wang, X. Wang and P. R. C. Gascoyne, *J. Electrost.*, 1997, **39**, 277.
51 S. S. Das, P. García-Sanchez, A. Ramos and G. Yossifon, *J. Colloids Sci.*, 2025, **686**, 118.
52 **https://imaris.oxinst.com/**.
53 T. Fischer, A. Hayn and C. T. Mierke, *Front. Cell Dev. Biol.*, 2020, **8**, 393.
54 E. Fischer-Friedrich, A. A. Hyman, F. Jülicher, D. J. Müller and J. Helenius, *Sci. Rep.*, 2014, **4**, 6213.